The Polar Summer Tropopause Inversion Layer

WILLIAM J. RANDEL AND FEI WU

National Center for Atmospheric Research, Boulder, Colorado*

(Manuscript received 30 December 2009, in final form 5 April 2010)

ABSTRACT

Temperature profiles in polar latitudes during summer reveal a strong and persistent inversion layer associated with the polar summer tropopause. This inversion layer is characterized by a temperature increase of ~8 K in the first 2–3 km above the tropopause and is observed throughout summer polar latitudes in both hemispheres. Radiosonde and GPS radio occultation temperature observations are used to document characteristics of the inversion layer, including its seasonal variability and modulation by synoptic meteorological systems (cyclones and anticyclones). Previous analyses have suggested a radiative mechanism for formation and maintenance of tropopause inversions, related to water vapor and ozone near the tropopause. Fixed dynamical heating (FDH) calculations are used herein to investigate this behavior in polar regions, based on observed seasonally varying profiles of water vapor (from satellite measurements) and ozone (from ozonesondes). Water vapor exhibits a strong seasonal cycle throughout the troposphere and lowest stratosphere, with a pronounced summer maximum, which is primarily a result of the seasonally varying tropospheric temperatures. The FDH calculations suggest that enhanced summer water vapor leads to strong radiative cooling in a narrow layer near the tropopause, so that the radiative influence of water vapor provides a primary mechanism for the summer inversion layer.

1. Introduction

The tropopause inversion layer (TIL) refers to a region of enhanced static stability above the extratropical tropopause, associated with a narrow-scale temperature inversion. The TIL was discovered in analysis of high-vertical-resolution radiosonde measurements by Birner et al. (2002) and Birner (2006), using a tropopause-based vertical coordinate system. Because of substantial variability in the height of the extratropical tropopause (linked to synoptic-scale eddies), the TIL structure is washed out when taking ground-based averages, whereas it is a ubiquitous and clear feature in tropopause coordinates. Global behavior of the TIL was analyzed using global positioning system (GPS) radio occultation data by Randel et al. (2007) and Grise et al. (2010), and also using radiosonde data by Bell and Geller (2008). These results showed that the TIL is a global phenomenon, evident over the midlatitudes of both hemispheres throughout the year. More recent work has highlighted a close link between the tropopause inversion and constituent gradients across the tropopause (Hegglin et al. 2009; Kunz et al. 2009). The GPS temperature data furthermore highlighted that the strongest TIL occurs over polar regions during summer (in both hemispheres); this finding is consistent with Zängl and Hoinka (2001) and Schmidt et al. (2005), who identify maximum tropopause sharpness (based on vertical temperature gradients) over both summer poles [this was also highlighted for the Arctic by Birner (2006)]. A strong polar summer TIL is also a feature observed in climate models, even ones with relatively low vertical resolution (Gettelman et al. 2010). One objective of this paper is to document observed characteristics of the polar summer TIL in further detail, including the spatial structure and seasonal variation, behavior of the different hemispheres, and relation to synoptic meteorological variability. We also explore a radiative forcing mechanism for the summer TIL, testing the influence of observed seasonal variations of water vapor and ozone using a fixed dynamical heating (FDH) methodology (Forster and Shine 2002). We note that at present the mechanisms that force and maintain the TIL are not well understood, and there are possible

* The National Center for Atmospheric Research is sponsored by the National Science Foundation.

Corresponding author address: William J. Randel, NCAR, P.O. Box 3000, Boulder, CO 80307–3000.
E-mail: randel@ucar.edu

DOI: 10.1175/2010JAS3430.1

contributions from dynamical (Birner 2006, 2010; Wirth 2004; Wirth and Szabo 2007; Son and Polvani 2007) and radiative effects (Randel et al. 2007; Kunz et al. 2009). Because the strongest TIL is observed during polar summer, this may be a period to improve fundamental understanding of forcing mechanisms.

2. Data and analysis

The data analyzed here include temperature profiles from radiosondes and GPS radio occultation, plus ozone and water vapor measurements (from ozonesondes and satellite data, respectively). For radiosonde data we focus on one station in the high Arctic (Eureka; 80°N, 86°W) and one station in Antarctica (Neumayer; 71°S, 8°W). The data are obtained from the World Ozone and Ultraviolet Radiation Data Center (available online at http://es-ee.tor.ec.gc.ca/cgi-bin/ozonesondeflights/) and were chosen because of the availability of frequent measurements and contemporaneous ozonesonde data. There are typically one or more observations per week for both of these stations (more frequent during winter and spring), with data at Eureka covering the years 1992–2007 and at Neumayer covering 1992–2008. We have also examined several other stations in the Arctic and Antarctic, and the results are very similar to those shown here for Eureka and Neumayer. All of our calculations regarding the tropopause are based on the standard World Meteorological Organization (WMO) lapse rate criterion.

We use GPS temperature data from the Constellation Observing System for Meteorology, Ionosphere, and Climate (COSMIC; Anthes et al. 2008), which have measurements covering the years 2006–09. The GPS temperature data are characterized by high vertical resolution and high accuracy over altitudes covering ~5–30 km. The vertical resolution is better than 1 km over these altitudes, and we use data oversampled on a 200-m vertical grid. For each hemisphere, there are typically 4000–6000 observations poleward of 60° during each month.

Ozone vertical profile measurements from ozonesondes are available for Eureka and Neumayer for the same sampling as the radiosonde data. For vertical profiles of water vapor we utilize the satellite measurements from the Atmospheric Chemistry Experiment Fourier Transform Spectrometer (ACE-FTS) instrument (Bernath et al. 2005). The ACE-FTS is a solar occultation measurement with irregular sampling but relatively frequent observations over polar latitudes. The vertical resolution of the ACE-FTS water vapor measurements is approximately 3 km, with the data oversampled on a 1-km grid. We use all of the available data from ACE-FTS over the years 2004–09 to build up a climatology of polar upper troposphere–lower stratosphere (UTLS) water vapor [with a total of approximately 4000 profiles over polar regions (60°–90°) of each hemisphere for the entire period]. Because of the irregular sampling of the ACE-FTS observations, we calculate monthly average profiles of water vapor in a tropopause-based coordinate system, using temperature profiles provided with the ACE-FTS retrievals (which typically show reasonable agreement with nearby GPS data). This tropopause-based analysis helps minimize variability associated with systematic latitudinal changes of the ACE-FTS sampling.

3. Mean structure and variability

a. Polar summer inversion climatology

An example of the vertical profile of summertime temperature from Eureka is shown in Fig. 1a. The tropopause is observed near 10 km, with a strong temperature increase (inversion) of ~8 K over the first few kilometers above the tropopause, followed by an approximately isothermal stratosphere above ~12 km. The inversion layer corresponds to a strong narrow maximum in static stability just above the tropopause, as quantified by the Brunt–Väisälä frequency N^2 shown in Fig. 1b. This strong maximum in N^2 over the summer pole was also identified in the climatological analysis of Birner (2006).

Figure 2 shows comparisons between polar summer temperatures from radiosondes and nearby GPS measurements for data at both Eureka (Fig. 2a, for the same profile as in Fig. 1) and Neumayer (Fig. 2b). Although the GPS measurements represent horizontal averages over ~200 km, there is good agreement between these data. Note that the profile at Neumayer (in the Antarctic summer) is very similar to the structure found at Eureka (during Arctic summer). These profiles with strong inversion layers are typical of the structure observed throughout the summer in both hemispheres.

The GPS data provide dense sampling to study the structure and variability of the polar summer (much more than isolated radiosonde observations). The ubiquitous nature of the summer TIL is demonstrated in Fig. 3, showing 20 profiles near 80°N (for a range of longitudes) on 26 July 2007. Each of the temperature profiles shows a structure similar to Figs. 1 and 2, albeit with some variation in the exact height of the tropopause and strength of the inversion. Much of this variability is linked to synoptic-scale meteorological structure, as shown below. The vertical scale of the inversion can be measured as the distance between the tropopause and the altitude where the lapse rate reaches 0 K (in the lower stratosphere), and statistics from the GPS and radiosonde

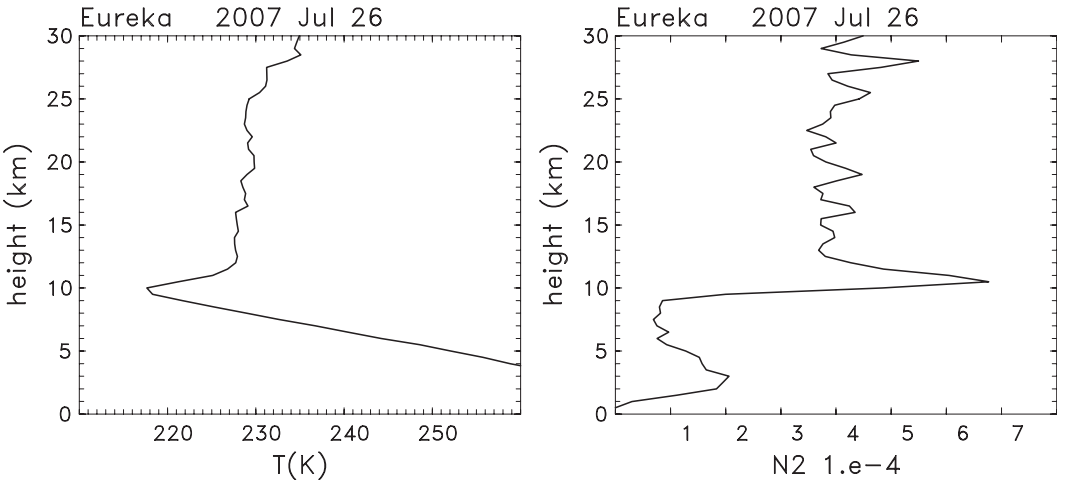

FIG. 1. (a) Radiosonde vertical temperature profile at Eureka on 26 Jul 2007. (b) Corresponding vertical profile of static stability (N^2, 10^{-4} s^{-2}).

measurements give a value of 2–3 km for this vertical scale.

Seasonal variation in strength of the polar TIL in both hemispheres is shown in Fig. 4, based on GPS observations. Here we use a tropopause-based coordinate system [i.e., the height of the lapse-rate tropopause Z_{LRT} is calculated for each individual profile] and calculate the strength of the inversion: $T(Z_{\mathrm{LRT}} + 2\ \mathrm{km}) - T(Z_{\mathrm{LRT}})$. This serves as a reasonable measure of the strength of the inversion, and these results are not sensitive to the exact choice of 2 km above the tropopause; we note that similar variability was shown for lapse rate calculations for the first kilometer above the tropopause for selected polar regions in Zängl and Hoinka (2001). The results in Fig. 4 are averaged over all available GPS data for the polar cap regions (70°–90°N and S), and there are typically ~100 GPS observations per day over both regions. The time series show maximum inversions in the Arctic of ~7–9 K, peaking during July–September (JAS), and similar maxima in the Antarctic during February–March (FM). There is an inversion layer (i.e., positive values in Fig. 4) for all months of the year in the Arctic (with small magnitude during winter months), whereas there is no inversion in the Antarctic during most of winter–spring (June–November). Figure 4 also shows similar calculations based on monthly average climatologies from the Eureka and Neumayer radiosonde data. Overall there is good agreement between the GPS and radiosonde-based results, in terms of both inversion amplitude and seasonal variability.

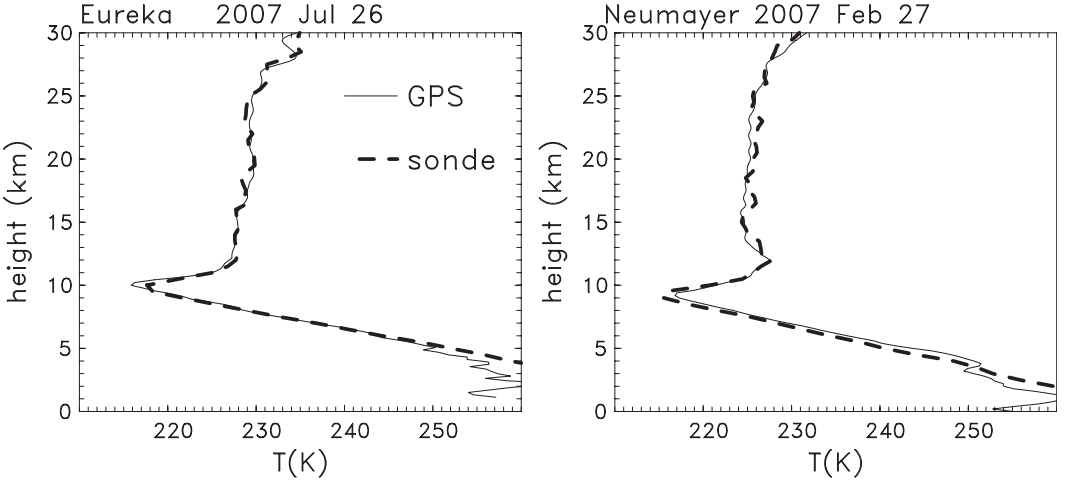

FIG. 2. Vertical profile of summertime temperature at (a) Eureka (26 Jul 2007) and (b) Neumayer (27 Feb 2007), comparing results from radiosondes and GPS.

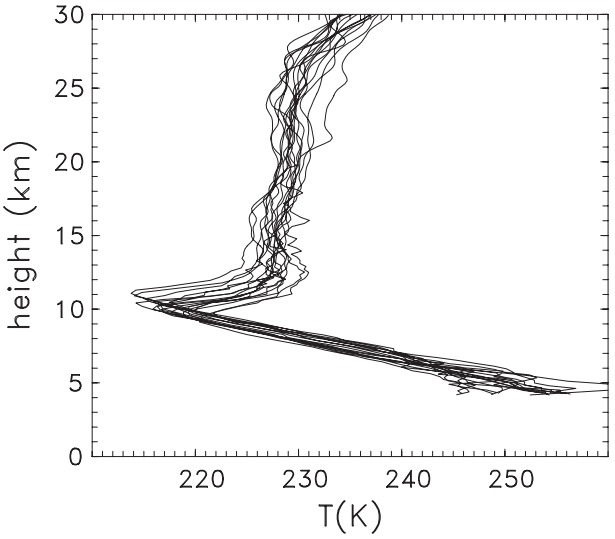

FIG. 3. GPS temperature profiles for observations over a range of longitudes near 80°N on 26 Jul 2007.

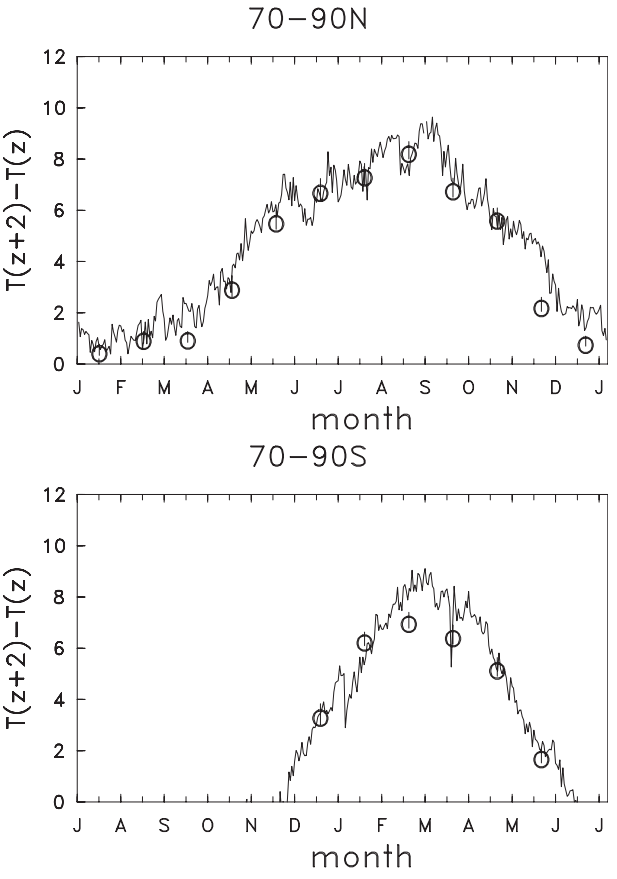

FIG. 4. Annual time series of daily average polar tropopause inversion strength [defined as $T(Z_{LRT} + 2\ km) - T(Z_{LRT})$, K] for the (a) Arctic (70°–90°N) and (b) Antarctic (70°–90°S). Time series are derived from an average of all COSMIC observations (typically 60 per day in each hemisphere). The circles denote corresponding climatological monthly average results based on (top) Eureka and (bottom) Neumayer radiosonde data. Note that the time axis in (b) runs from July to June.

The latitudinal structure of summer inversion strength is illustrated in Fig. 5, showing GPS measurements of $T(Z_{LRT} + 2\ km) - T(Z_{LRT})$ binned as a function of latitude for NH summer (July–September) and SH summer (February–March) statistics (these months are chosen based on the largest polar inversions, as shown Fig. 4). This comparison shows a remarkably similar behavior in both hemispheres, with the inversion strength systematically increasing from low to high latitudes (from ~1 to ~8 K). The strongest inversion occurs over latitudes poleward of 70°, and there is relatively little time average longitudinal structure in the polar TIL found in either hemisphere (results not shown here).

A climatology of Arctic polar temperatures, static stability (N^2), and ozone at Eureka is shown in Fig. 6, constructed from observations averaged over 1992–2007 (in ground-based coordinates). The mean tropopause is also indicated in Fig. 6, showing a stable average altitude of 9–10 km over the year. The strong summer TIL is identified by the maximum N^2 values near 10 km during approximately May–October, with a corresponding temperature inversion found in the temperature plot. Ozone is plotted in density units [Dobson units (DU) per kilometer], showing a strong seasonal cycle in the lower stratosphere peaking during boreal spring, with a systematic reduction during summer, which is primarily due to photochemical relaxation (e.g., Fioletov and Shepherd 2005). There is not an apparent relation between seasonal variations of the TIL and ozone in the lower stratosphere.

An equivalent climatology for the Antarctic is shown in Fig. 7 for observations at Neumayer, averaged over 1992–2008. Here there is a more well-defined seasonal variation in the height of the tropopause, varying from ~9 km in summer to ~11.5 km in winter. In terms of stability (N^2), the strongest TIL occurs above the summer tropopause during January–March. The seasonally evolving temperatures, which warm first at higher altitudes in the stratosphere, also result in an enhanced stability region above 15 km during Antarctic spring (October–January). Ozone evolution in the Antarctic in Fig. 7 is very different from the Arctic because of the occurrence of minimum values in the lower stratosphere during spring (September–October) associated with the Antarctic ozone hole.

Seasonal behavior of the polar tropopause has recently been investigated by Tomikawa et al. (2009), comparing thermal structure and seasonal variations using ground-based, thermal-tropopause-based, and ozone-tropopause-based coordinates. They note a summertime

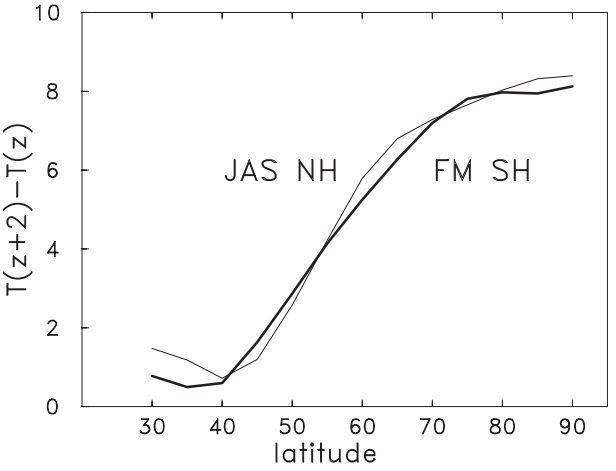

FIG. 5. Latitudinal structure of the tropopause inversion strength [defined as $T(Z_{LRT} + 2\text{ km}) - T(Z_{LRT})$, K] for COSMIC observations in 5° latitude bins during NH summer (JAS) and SH summer (FM).

maximum in lower stratospheric stability (i.e., a TIL) in both hemispheres, similar to the results shown here, and demonstrate that it is a robust feature in each coordinate system.

b. Meteorological variability

Randel et al. (2007) demonstrated systematic variability in the strength of the TIL over midlatitudes related to synoptic meteorological structure: anticyclonic circulation systems exhibit stronger inversions (typically ~5 K) than cyclonic flow (~2 K). This behavior is consistent with that expected for balanced dynamics, as shown by Wirth (2003). We have explored similar behavior during polar summer, based on binning July–September 2007 GPS observations over 70°–90°N according to the 200-hPa relative vorticity derived from National Centers for Environmental Prediction (NCEP) meteorological analyses (following the methodology of Randel et al. 2007). The statistical distribution of relative vorticity ζ over the polar cap (not shown here) is similar to that found over midlatitudes (Randel et al. 2007), with a Gaussian-shaped distribution of vorticity ($-5 \times 10^{-5} < \zeta < 5 \times 10^{-5}$ s^{-1}) centered slightly to the cyclonic side (with a central value of $\sim 1 \times 10^{-5}$ s^{-1}). Figure 8a shows the tropopause altitude for the GPS observations binned according to vorticity, which shows systematic structure of higher altitudes (11 km and above) for strongly anticyclonic flow to lower altitudes (~9 km) for cyclonic circulation. This is similar to polar tropopause behavior shown by Zängl and Wirth (2002) and is consistent with theoretical expectations (Hoskins et al. 1985). The strength of the polar TIL binned according to vorticity is shown in Fig. 8b,

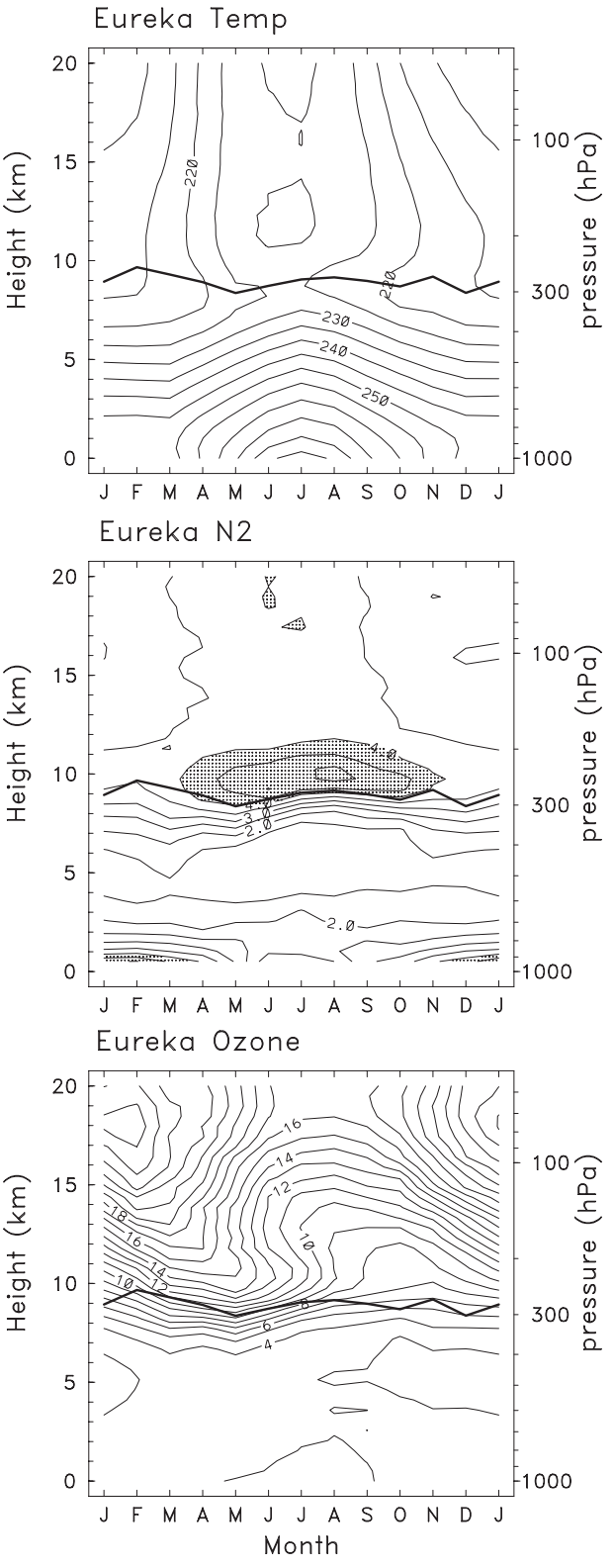

FIG. 6. Climatological seasonal variation of (a) temperature (K), (b) N^2 (10^{-4} s^{-2}), and (c) ozone density (DU km^{-1}) for the Arctic (from Eureka observations over 1992–2007). The tropopause is denoted as a thick line in each panel.

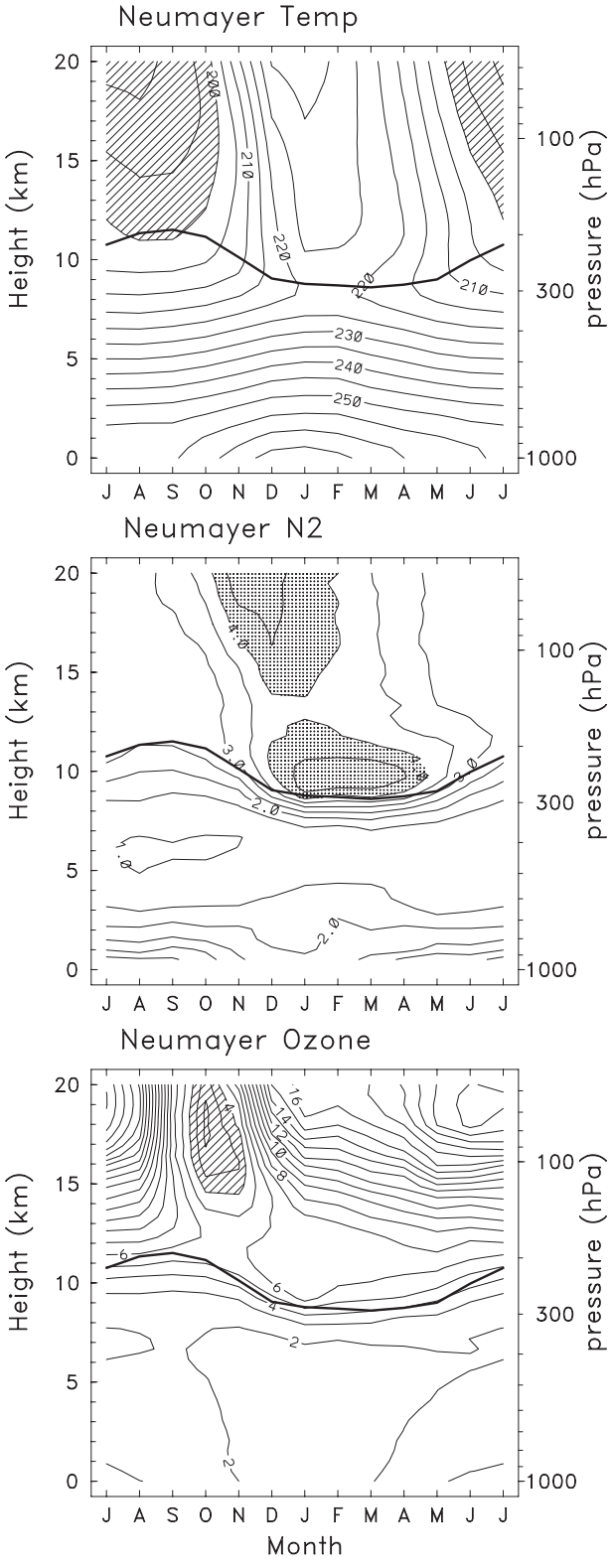

FIG. 7. As in Fig. 6, but for the Antarctic (from Neumayer data during 1992–2008). Note that the time axis runs from July to June.

revealing a systematic variation with the strongest inversions (~9 K) for anticyclonic flow and weaker ones (~5 K) for the strongest cyclones; there is a ~8-K average inversion for near-zero vorticity. This overall behavior is very similar to midlatitudes (Randel et al. 2007), with the main difference being an overall increase of the average TIL strength for the polar summer. These results demonstrate that the polar summer TIL is modulated by synoptic meteorological structure (as expected), but these are relatively weak modulations on the strong TIL (~8 K) that exists as a persistent background.

4. Radiative forcing of the polar summer TIL

Randel et al. (2007) hypothesized a radiative forcing mechanism for the TIL, based on the combined effects of water vapor and ozone near the tropopause, and Kunz et al. (2009) demonstrated a strong influence of water vapor on radiative cooling in the tropopause region. Here we explore these radiative effects for the polar summer, based on FDH calculations incorporating observed water vapor and ozone profiles. Figure 9a shows the monthly variation of water vapor mixing ratio at the altitude of the tropopause over the Arctic (60°–90°N) derived from binned ACE-FTS observations for the years 2004–09 (using tropopause coordinates, as noted in section 2). These data show a large seasonal variation, with minimum mixing ratios in winter (~25 ppmv) and maximum in summer (~60 ppmv). Note that the ACE-FTS sampling does not provide observations for every month, but the overall behavior is clear. Figure 9b shows the vertical profile of water vapor for the ACE-FTS data binned according to 3-month seasons [December–February (DJF), etc.], and here the ACE-FTS data in tropopause coordinates have been converted to altitude coordinates using a mean Arctic tropopause altitude of 9 km. Figure 9b highlights the strong seasonal variation throughout the troposphere into the lowermost stratosphere (several kilometers above the tropopause, near 9 km). There is a relatively small seasonal variation above 12 km, with a summertime polar minimum over ~12–16 km related to transport of dry stratospheric air from tropical latitudes (Randel et al. 2001). Calculation of the upper tropospheric relative humidity (using climatological temperatures as in Fig. 6) shows relatively constant values (~50%) in the polar upper troposphere throughout the year, so that the large summer water vapor mixing ratios (specific humidity) seen in Fig. 9 are mainly following the warm summer polar tropospheric temperatures, throughout the more or less well-mixed troposphere. The extension of the tropospheric water vapor variations several kilometers above the tropopause

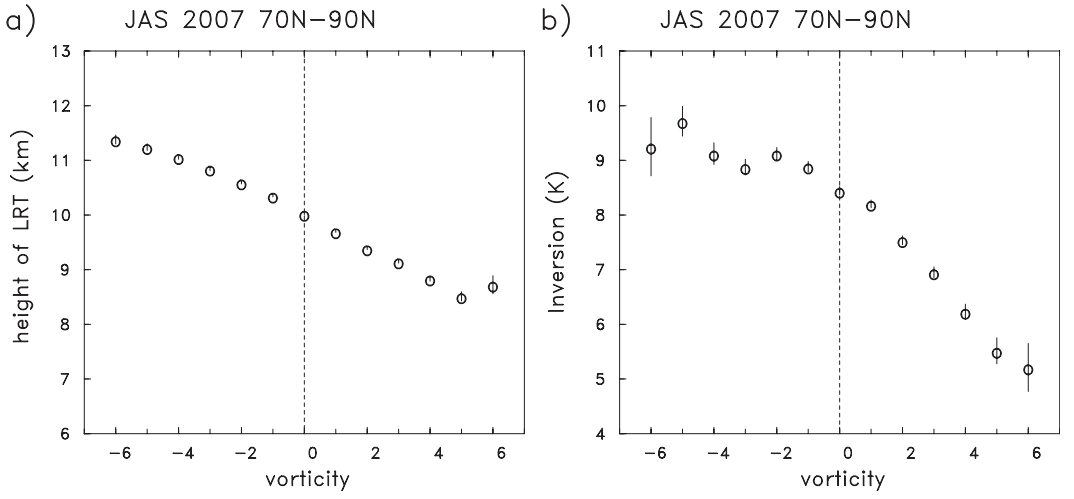

FIG. 8. (a) Average altitude of the polar tropopause derived from the COSMIC temperature profiles, binned as a function of collocated ζ (10^{-5} s^{-1}) at 200 hPa (from NCEP reanalysis data). (b) Average strength of the polar tropopause inversion [defined as $T(Z_{\mathrm{LRT}} + 2\ \mathrm{km}) - T(Z_{\mathrm{LRT}})$, K], calculated within each vorticity bin.

is an aspect of water vapor observed throughout the extratropics in aircraft observations (Pan et al. 2004) and previously documented in ACE-FTS data by Hegglin et al. (2009); this is a well-known aspect of the so-called extratropical tropopause mixing layer (Hoor et al. 2002; Kunz et al. 2009). We note that these ACE-FTS data (with vertical resolution ~3 km) may provide a slightly smoothed estimate of the water vapor transition layer above the tropopause.

The seasonal average ozone values from Eureka (i.e., the values from Fig. 6) are shown in Fig. 10, and these are used as input to the FDH calculations below. These show the expected behavior of maxima during winter–spring and minima in summer–autumn. There are relatively large relative variations in the region near and above the tropopause.

The FDH calculations follow the methodology of Forster and Shine (2002) and examine the effects of observed seasonal changes in water vapor (Fig. 9) and ozone (Fig. 10) on polar temperatures. As a background we use the annual mean temperature profile from Eureka radiosondes (and the overall results are not sensitive to the choice of background season). We calculate the FDH temperature changes associated with the different seasonal profiles of water vapor (from Fig. 9) and ozone (Fig. 10) based on summertime radiative exposure. Figure 11a

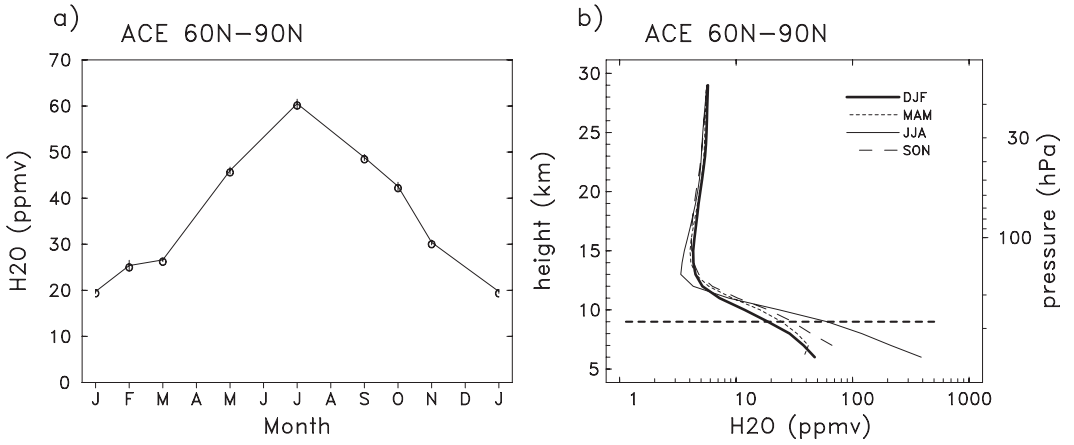

FIG. 9. (a) Monthly average water vapor mixing ratio (ppmv) at the altitude of the tropopause over the Arctic (60°–90°N) derived from ACE-FTS data during 2004–09. The circles show the average values; the vertical bars denote the standard deviation. (b) Vertical profile of ACE-FTS water vapor mixing ratio (ppmv) for seasonal averages (DJF, etc.), calculated in tropopause coordinates and transformed to altitude using a mean tropopause altitude of 9 km (noted with the heavy dashed line).

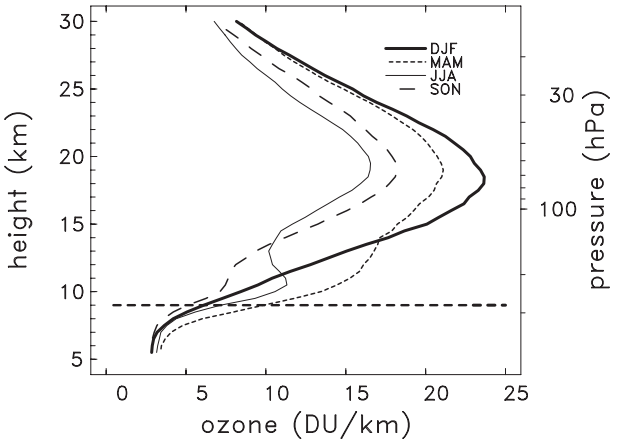

FIG. 10. Vertical profiles of seasonal average ozone density (DU km^{-1}) from the climatology at Eureka. The horizontal line denotes the average tropopause altitude.

shows the FDH temperature response to water vapor changes, with results for the different seasons compared to the (minimum) water vapor values during winter (DJF); Fig. 11b shows the corresponding temperature differences. The results show that water vapor increases near the tropopause result in strong cooling, and the effects are particularly strong during summer (with FDH temperature differences up to 15 K). The peak of this cooling occurs near 10 km, and the overall thermal structure for the summer water vapor case in Fig. 11a shows a marked minimum near 10 km, similar to the observed structure (i.e., Figs. 1–3).

It should be noted that the FDH estimates are highly idealized calculations, intended to test the sensitivity of temperature to constituent changes rather than to calculate exact temperature profiles. For example, the magnitude of the June–August (JJA) temperature inversion in Fig. 11a (~10 K) is somewhat larger than observed (~8 K), and the upper tropospheric lapse rate substantially exceeds a dry adiabat (and would presumably be alleviated by dynamical processes). In spite of these differences, the FDH results capture the key aspects of the polar inversion, including the seasonal behavior and approximate vertical structure.

The calculations testing ozone sensitivity are shown in Fig. 12. The FHD temperature changes associated with seasonal ozone variations are relatively small, typically <1 K (Fig. 12b), and are more or less in phase with the ozone changes [i.e., the increase in lower stratosphere ozone from DJF to March–May (MAM) provides relative warming]. However, the small temperature changes in Fig. 12 suggest that ozone is much less important than water vapor (Fig. 11) for the temperature structure near the polar tropopause. Overall, the observations of the strong seasonal maximum in water vapor during summer coincident with the enhanced TIL, together with the explicit FDH calculations, suggest that the radiative influence of water vapor plays a strong role in forming and maintaining the polar summer TIL.

5. Summary and discussion

Radiosonde and GPS observations have demonstrated that the TIL is a ubiquitous feature of the extratropical tropopause region, with strongest amplitude in summer polar regions (Birner 2006; Randel et al. 2007; Grise et al. 2010). Here we have focused on quantifying the detailed behavior of the polar summer TIL, including its space–time structure and variability. Our observations show a persistent summertime inversion layer immediately

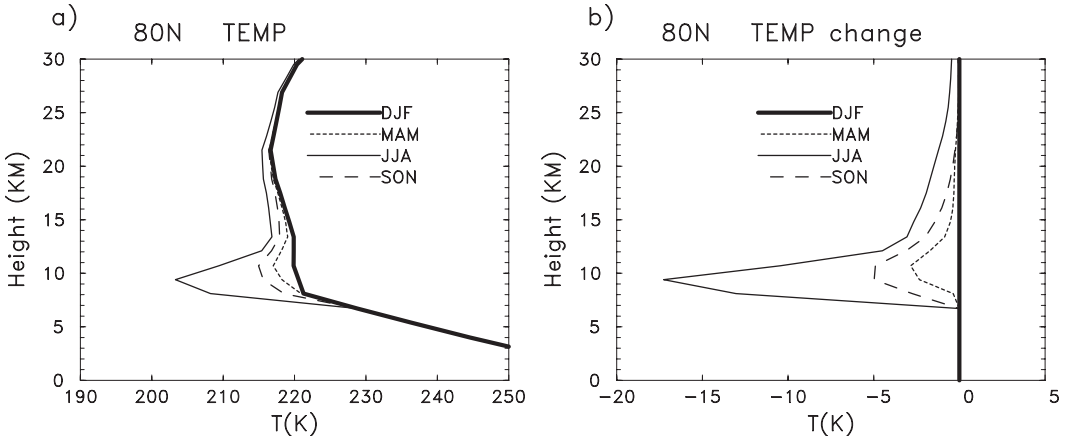

FIG. 11. (a) Fixed dynamical heating temperature response to the seasonal water vapor variations shown in Fig. 9b. Thick black curve shows the background reference temperatures with DJF water vapor, and the other curves show the corresponding temperatures for imposed water vapor from MAM, JJA, and September–November (SON). (b) The corresponding temperature differences from DJF.

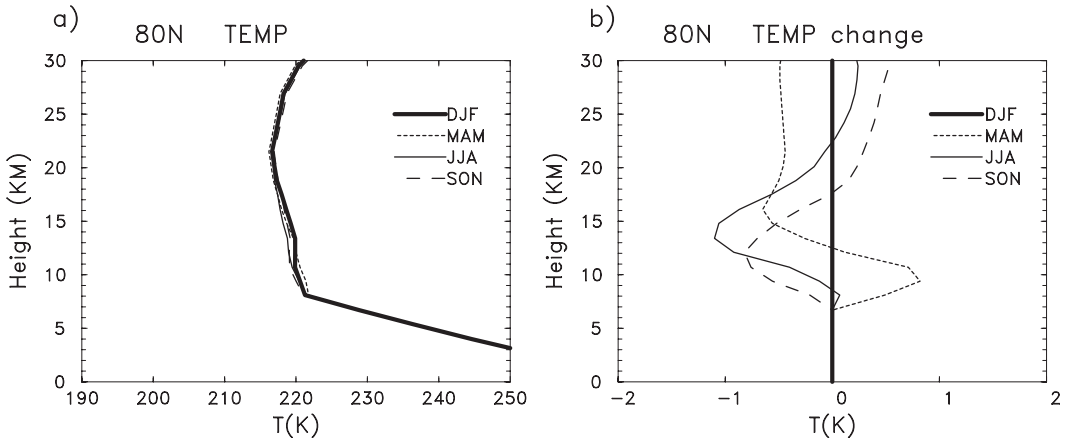

FIG. 12. Fixed dynamical heating calculations of temperature response to seasonal ozone variations shown in Fig. 10 (with details similar to Fig. 11): (a) the temperature structures; (b) the differences from DJF.

above the polar tropopause, with an average inversion strength of ~8 K. The vertical structure and the latitudinal and temporal characteristics of the polar TIL are similar between the hemispheres, suggesting this is a fundamental aspect of the polar summer circulation. GPS observations show that the polar TIL is modulated by synoptic meteorological variability (similar to midlatitudes), but this produces a relatively small modulation on the persistent background inversion.

We have explored the radiative forcing of the polar TIL due to seasonal variations in water vapor and ozone, based on FDH calculations. Water vapor exhibits a strong seasonal variation over polar latitudes, with a pronounced summer maximum throughout the troposphere and lowest stratosphere. The high values of tropospheric water vapor (which mainly follow the seasonal tropospheric temperatures) extend for the first few kilometers above the tropopause before merging with the extremely dry air (~3 ppmv) characteristic of the stratosphere (above 12 km in Fig. 11b). This vertical structure is a characteristic of the extratropical tropopause mixing layer (Pan et al. 2004; Hegglin et al. 2009; Kunz et al. 2009), with the result that water vapor at the tropopause lies midway between troposphere and stratosphere values. The FDH calculations show that the large summer maximum in water vapor is associated with strong cooling near the tropopause (~10 km), with a resulting temperature structure that closely resembles the observed behavior. The corresponding calculations incorporating seasonal ozone variations (Fig. 12) show relatively little effect (temperature changes < 1 K). We conclude that the radiative effects of water vapor are a major contributor to the formation and maintenance of the polar summer TIL, and this helps explain why models with

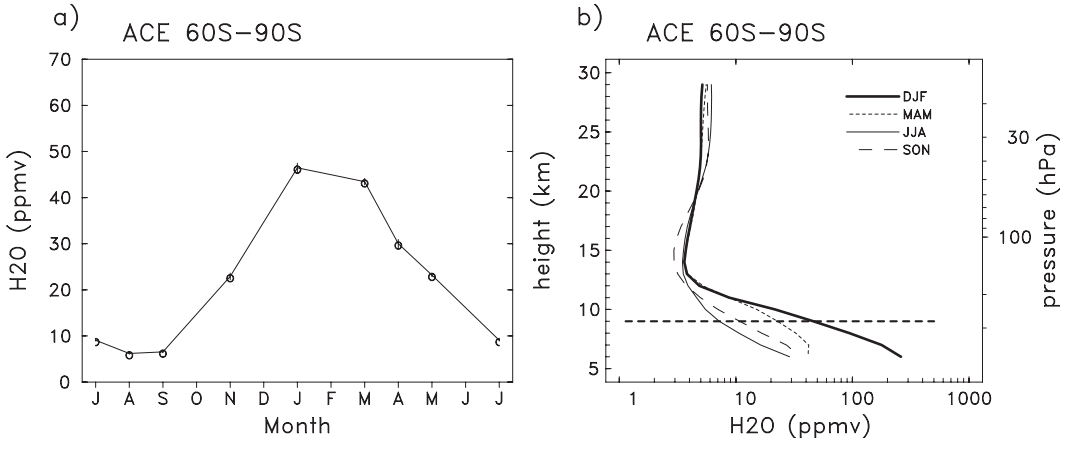

FIG. 13. (a) Monthly average water vapor mixing ratio (ppmv) at the altitude of the tropopause over the Antarctic (60°–90°S) derived from ACE-FTS data during 2004–09. Note that the time axis is shifted by 6 months compared to Fig. 9a. (b) Vertical profile of ACE-FTS water vapor mixing ratio (ppmv) over the Antarctic for seasonal averages (DJF, etc.). Calculation details are as in Fig. 9.

relatively low vertical resolution can capture this behavior (Gettelman et al. 2010). We note that a similar summertime maximum in water vapor near the tropopause is observed over the Antarctic (Fig. 13), and FHD calculations (not shown here) suggest a radiative effect similar to that shown for the Arctic in Fig. 11b. Hence this mechanism is a reasonable explanation for the observed hemispheric symmetry of the polar summer TIL.

While Randel et al. (2007) suggested that the radiative effects of both water vapor and ozone could contribute to formation and maintenance of the TIL, the results shown here for polar summer clearly highlight a dominant role for water vapor. This agrees with the calculations of Kunz et al. (2009), who demonstrate a major radiative influence for water vapor in the midlatitudes. A key role for water vapor in the TIL was also highlighted by Hegglin et al. (2009), who emphasized similarity between TIL structure and water vapor vertical gradients near the tropopause. These consistent results suggest an updated perspective that the radiative effects of water vapor near the tropopause may be a dominant mechanism for the TIL.

Acknowledgments. We thank Thomas Birner, Piers Forster, Laura Pan, and Andrew Gettelman for discussions during the course of this work and comments on the manuscript. We also thank two anonymous reviewers for suggestions that helped improve the paper. The GPS temperature retrievals were processed by the University Corporation for Atmospheric Research (UCAR). This work was partially supported by the NASA ACMAP Program. The National Center for Atmospheric Research is operated by the University Corporation for Atmospheric Research, under sponsorship of the National Science Foundation.

REFERENCES

Anthes, R. A., and Coauthors, 2008: The COSMIC/FORMOSAT-3 Mission: Early results. *Bull. Amer. Meteor. Soc.,* **89,** 313–333.

Bell, S. W., and M. A. Geller, 2008: Tropopause inversion layer: Seasonal and latitudinal variations and representation in standard radiosonde data and global models. *J. Geophys. Res.,* **113,** D05109, doi:10.1029/2007JD009022.

Bernath, P. F., and Coauthors, 2005: Atmospheric Chemistry Experiment (ACE): Mission overview. *Geophys. Res. Lett.,* **32,** L15S01, doi:10.1029/2005GL022386.

Birner, T., 2006: Fine-scale structure of the extratropical tropopause region. *J. Geophys. Res.,* **111,** D04104, doi:10.1029/2005JD006301.

——, 2010: Residual circulation and tropopause structure. *J. Atmos. Sci.,* **67,** 2582–2600.

——, A. Dörnbrack, and U. Schumann, 2002: How sharp is the tropopause at midlatitudes? *Geophys. Res. Lett.,* **29,** 1700, doi:10.1029/2002GL015142.

Fioletov, V. E., and T. G. Shepherd, 2005: Summertime total ozone variations over middle and polar latitudes. *Geophys. Res. Lett.,* **32,** L04807, doi:10.1029/2004GL022080.

Forster, P. M., and K. P. Shine, 2002: Assessing the climate impact of trends in stratospheric water vapor. *Geophys. Res. Lett.,* **29,** 1086, doi:10.1029/2001GL013909.

Gettelman, A., and Coauthors, 2010: Multi-model assessment of the upper troposphere and lower stratosphere: Tropics and trends. *J. Geophys. Res.,* in press.

Grise, K., D. Thompson, and T. Birner, 2010: A global survey of static stability in the stratosphere and upper troposphere. *J. Climate,* **23,** 2275–2292.

Hegglin, M. I., C. D. Boone, G. L. Manney, and K. A. Walker, 2009: A global view of the extratropical tropopause transition layer from Atmospheric Chemistry Experiment Fourier Transform Spectrometer O_3, H_2O, and CO. *J. Geophys. Res.,* **114,** D00B11, doi:10.1029/2008JD009984.

Hoor, P., H. Fischer, L. Lange, J. Lelieveld, and D. Brunner, 2002: Seasonal variations of a mixing layer in the lowermost stratosphere as identified by the CO–O_3 correlation from in situ measurements. *J. Geophys. Res.,* **107,** 4044, doi:10.1029/2000JD000289.

Hoskins, B. J., M. E. McIntyre, and A. W. Robertson, 1985: On the use and significance of isentropic potential vorticity maps. *Quart. J. Roy. Meteor. Soc.,* **111,** 877–946.

Kunz, A., P. Konopka, R. Müller, L. L. Pan, C. Schiller, and F. Rohrer, 2009: High static stability in the mixing layer above the extratropical tropopause. *J. Geophys. Res.,* **114,** D16305, doi:10.1029/2009JD011840.

Pan, L. L., W. J. Randel, B. L. Gary, M. J. Mahoney, and E. J. Hintsa, 2004: Definitions and sharpness of the extratropical tropopause: A trace gas perspective. *J. Geophys. Res.,* **109,** D23103, doi:10.1029/2004JD004982.

Randel, W. J., F. Wu, A. Gettelman, J. M. Russell, J. M. Zawodny, and S. J. Oltmans, 2001: Seasonal variation of water vapor in the lower stratosphere observed in Halogen Occultation Experiment data. *J. Geophys. Res.,* **106,** 14 313–14 326.

——, ——, and P. Forster, 2007: The extratropical tropopause inversion layer: Global observations with GPS data, and a radiative forcing mechanism. *J. Atmos. Sci.,* **64,** 4489–4496.

Schmidt, T., S. Heise, J. Wickert, G. Beyerle, and C. Reigber, 2005: GPS radio occultation with CHAMP and SAC-C: Global monitoring of thermal tropopause parameters. *Atmos. Chem. Phys.,* **5,** 1473–1488.

Son, S.-W., and L. M. Polvani, 2007: Dynamical formation of an extra-tropical tropopause inversion layer in a relatively simple general circulation model. *Geophys. Res. Lett.,* **34,** L17806, doi:10.1029/2007GL030564.

Tomikawa, Y., Y. Nishimura, and T. Yamanouchi, 2009: Characteristics of tropopause and tropopause inversion layer in the polar region. *SOLA,* **5,** 144–144, doi:10.2151/sola.2009-036.

Wirth, V., 2003: Static stability in the extratropical tropopause region. *J. Atmos. Sci.,* **60,** 1395–1409.

——, 2004: A dynamical mechanism for tropopause sharpening. *Meteor. Z.,* **13,** 477–484.

——, and T. Szabo, 2007: Sharpness of the extratropical tropopause in baroclinic life cycle experiments. *Geophys. Res. Lett.,* **34,** L02809, doi:10.1029/2006GL028369.

Zängl, G., and K. P. Hoinka, 2001: The tropopause in the polar regions. *J. Climate,* **14,** 3117–3139.

——, and V. Wirth, 2002: Synoptic-scale variability of the polar and subpolar tropopause: Data analysis and idealized PV inversions. *Quart. J. Roy. Meteor. Soc.,* **128,** 2301–2315.